How Accurately Can Warm Rain Realistically Be Retrieved with Satellite Sensors? Part I: DSD Uncertainties

Richard M. Schulte,[a] Christian D. Kummerow,[a] Christian Klepp,[b] and Gerald G. Mace[c]

[a] *Department of Atmospheric Science, Colorado State University, Fort Collins, Colorado*
[b] *Max Planck Institute for Meteorology, Hamburg, Germany*
[c] *Department of Atmospheric Science, University of Utah, Salt Lake City, Utah*

ABSTRACT: A significant part of the uncertainty in satellite-based precipitation products stems from differing assumptions about drop size distributions (DSDs). Satellite radar-based retrieval algorithms rely on DSD assumptions that may be overly simplistic, whereas radiometers further struggle to distinguish cloud water from rain. We utilize the Ocean Rainfall and Ice-phase Precipitation Measurement Network (OceanRAIN), version 1.0, dataset to examine the impact of DSD variability on the ability of satellite measurements to accurately estimate rates of warm rainfall. We use the binned disdrometer counts and a simple model of the atmosphere to simulate observations for three satellite architectures. Two are similar to existing instrument combinations on the GPM *Core Observatory* and *CloudSat*, and the third is a theoretical triple-frequency radar–radiometer architecture. Using an optimal estimation framework, we find that the assumed DSD shape can have a large impact on retrieved rain rate. A three-parameter normalized gamma DSD model is sufficient for describing and retrieving the DSDs observed in the OceanRAIN dataset. Assuming simpler single-moment DSD models can lead to significant biases in retrieved rain rate, on the order of 100%. Differing DSD assumptions could thus plausibly explain a large portion of the disagreement in satellite-based precipitation estimates.

KEYWORDS: Rainfall; Algorithms; Satellite observations

1. Introduction

Warm-rain processes are an important part of the hydrologic cycle, especially over the oceans where aerosol concentrations tend to be low (Kubar et al. 2009). Observations from the *CloudSat* W-band satellite radar (Stephens et al. 2002) indicate that any given oceanic point may be beneath warm clouds between 10% and 50% of the time, with 20%–40% of these clouds containing rain or drizzle at the lowest *CloudSat* range bin (Nuijens et al. 2017). The probability of precipitation is lower than this, due to evaporation below cloud base. For example, Yang et al. (2018) found drizzle in over 80% of marine stratocumulus cloud profiles at Graciosa Island, but precipitation reached the surface in only about 30% of the profiles. Nuijens et al. (2017) find that the greatest warm cloud fractions occur on the east side of the ocean basins as well as to a lesser extent over the Southern Ocean. Uncertainties in how the prevalence of low, warm clouds will change as the climate warms is one of the largest sources of uncertainty in global climate projections (e.g., Zelinka et al. 2020; Mülmenstädt et al. 2021), and several studies (Trenberth and Fasullo 2010; Bodas-Salcedo et al. 2014; Kay et al. 2016; Hyder et al. 2018) have noted that the Southern Ocean energy balance is poorly represented in global climate models. In this context, accurate present-day estimates of precipitation, cloud water, and cloud fraction from satellites are very important for evaluating and constraining weather and climate models.

While the overall uncertainty in the global mean precipitation rate is on the order of 10% (Haynes et al. 2009; Stephens et al. 2012), the uncertainty is even greater near the poles (Adler et al. 2003; Andersson et al. 2011; Behrangi et al. 2016). One factor that likely contributes is uncertain and simplistic assumptions about drop size distributions (DSDs) for rainfall retrieval methods. Many radar-based precipitation retrieval algorithms assume a fixed DSD parameterization with only one free parameter (e.g., Haynes et al. 2009), or else merely choose between two sets of fixed parameters based on whether the precipitation is judged to be convective or stratiform (Lebsock and L'Ecuyer 2011; Duncan et al. 2018). The Global Precipitation Measurement mission (GPM) combined algorithm is more flexible, with two free parameters, but still prescribes a constant shape parameter (Grecu et al. 2016). In reality, drop sizes do not conform to arbitrary categories but rather exist on a spectrum. Meanwhile, radiometers are much more sensitive to the total water mass in the atmospheric column than the size of the drops, so cloud/rain partitioning is a major challenge (Elsaesser et al. 2017; Greenwald et al. 2018).

Historically, the relationships prescribed in satellite precipitation algorithms have often been based on precipitation observations made over continents or in tropical locations. However, recent field campaigns have provided insightful observations at more diverse locations, including regions where warm-rain processes are very important. The Observations of Aerosols above Clouds and Their Interactions project (ORACLES; Redemann et al. 2021) involved many aircraft flights observing cloud structure and precipitation characteristics over the southeast Atlantic Ocean (Dzambo et al. 2019). Retrievals combining W-band radar reflectivities with polarimeter measurements were performed to jointly estimate cloud water path and rainwater path, with cloud water path uncertainty on the order of 30% but with rainwater path

Distribution of OceanRAIN Observations
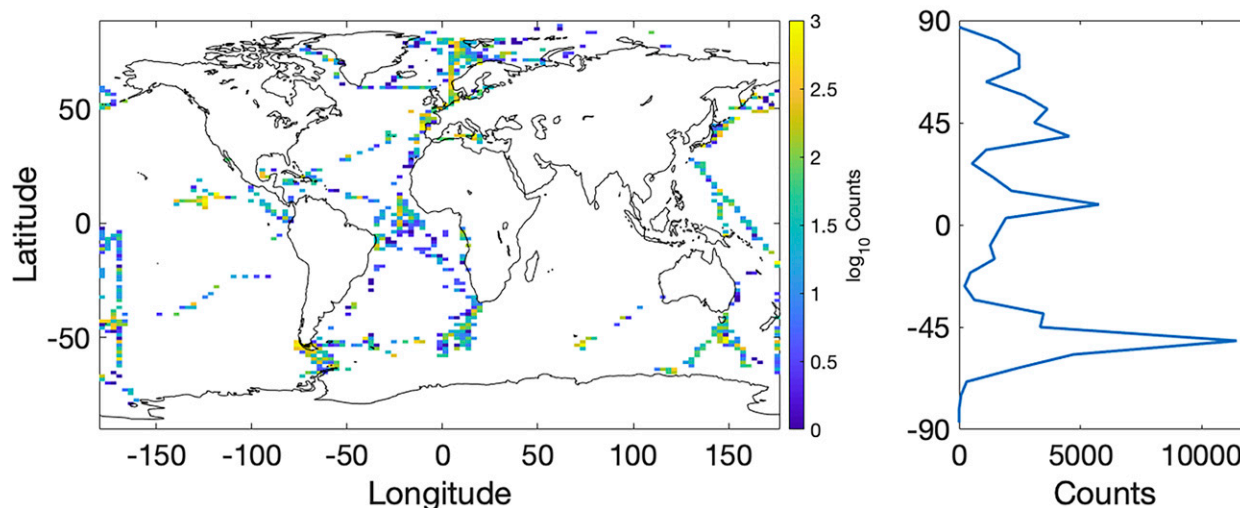

FIG. 1. Distribution of OceanRAIN DSD observations used in this study: (left) The spatial distribution, gridded on a 3° (longitude) by 1.5° (latitude) grid and colored according to the $\log_{10}$ of the number of 1-min observations within each grid box, and (right) a one-dimensional histogram with observations summed across each latitude band in 6° increments.

uncertainties frequently over 100% (Dzambo et al. 2021). The Cloud System and Evolution in the Trades campaign (CSET; Albrecht et al. 2019) included the deployment of a W-band airborne radar and a lidar to retrieve shallow cumulus cloud structures and precipitation. Sarkar et al. (2020) reported that rain drop distributions in CSET tended to shift toward larger drops sizes as the boundary layer deepened, and Sarkar et al. (2021) found that cumulus rain rates retrieved from the combined radar–lidar observations tended to be lower than in situ cloud probe measurements, in large part because the assumed raindrop size distribution was too narrow. In the Southern Ocean, a series of coordinated projects between 2016 and 2018 measured precipitation properties using in situ probes, radar, lidar, and other instruments (McFarquhar et al. 2021).

There has also been much work to validate and improve the DSD relationships assumed in satellite precipitation algorithms. The version-06A GPM precipitation algorithms are documented extensively in Seto et al. (2021). An important difference relative to earlier algorithm versions is the use of a DSD constraint that relates the rain rate to the mean drop diameter ($R–D_m$ relation). Liao et al. (2020) examined DSD data from several NASA field campaigns and arrived at a slightly different $R–D_m$ relation. They found that deviation from the $R–D_m$ relation was explained primarily by differences in the normalized intercept gamma parameter N_W. Shipboard observations from the Ocean Rainfall and Ice-phase Precipitation Measurement Network (OceanRAIN; Klepp et al. 2018) demonstrate significant latitudinal variability in oceanic rainfall properties, including the $R–D_m$ relation (Protat et al. 2019a).

Several studies have explored how DSD assumptions affect rain rates retrieved from ground-based radars (e.g., Lee and Zawadzki 2005; Adirosi et al. 2014; van de Beek et al. 2016). Fewer authors, however, have quantified the uncertainty in

satellite precipitation products resulting from their assumptions about DSDs. Lebsock and L'Ecuyer (2011) showed that the assumption of a Marshall–Palmer DSD as opposed to a drizzle DSD increased the mean retrieved rain rate in the *CloudSat* level-2C rain profile product (2C-RAIN-PROFILE) algorithm by a factor of 2 but tested no other DSD parameterizations. For the Global Precipitation Measurement Dual-Frequency Precipitation Radar (GPM DPR), Liao et al. (2014) found that using a dual-wavelength technique is able to generally keep estimates of retrieved rain rate within 10% of the true value, but only for rain rates greater than about 5 mm h^{-1}. More recent studies have reported mixed results. Protat et al. (2019b) speculate that high-latitude rain-rate retrievals from GPM could be significantly biased because of erroneous DSD assumptions, while Bringi et al. (2021) conclude that the current DSD assumptions "are not a major source of uncertainty" in the GPM combined algorithm.

Our study is distinct from earlier efforts in that it comprehensively and quantitatively estimates the impact of DSD assumptions in satellite precipitation retrieval algorithms. In addition, rather than focus on one particular instrument, we study how the DSD-related retrieval uncertainties change for different theoretical satellite architectures. This is important, as future satellite precipitation missions will have to make choices about what types of instruments to include. We construct simulated satellite observations based on surface disdrometer measurements and develop an optimal estimation retrieval algorithm to retrieve DSD parameters using various combinations of satellite measurements (section 3). We then investigate how retrieval errors are affected by sensor uncertainties and detection limits (section 4a), ancillary assumptions about the atmospheric profile (Section 4b), and the limitations of mathematical models to adequately capture the

TABLE 1. Selected radar specifications for the three theoretical satellite architectures that are considered in this study.

	Radar frequency (GHz)	PIA uncertainty (dBZ)	Z baseline uncertainty[a] (dBZ)	Z threshold (dBZ)	Radar integration time (ms)
Satellite A (similar to *CloudSat*)	94.0	1.25	1.0	−30.0	160.0
Satellite B (similar to GPM)	13.6	1.25	1.0	12.0	29.0
	35.5	1.25	1.0	12.0	42.0
Satellite C (triple frequency)	13.6	1.25	1.0	0.0	29.0
	35.5	1.25	1.0	0.0	42.0
	94.0	1.25	1.0	−50.0	160.0

[a] The reflectivity uncertainty is just a minimum value because the true value also depends on the difference between the measured Z and the Z threshold T, the radar integration time I, and the radar pulse repetition frequency F (4.3 m s^{-1} for all three satellites). The equation for the reflectivity uncertainty U is then given by $U = (N^2 + \{(4.343/\sqrt{IF})[1.0 + 10^{0.1(T-Z)}]\}^2)^{1/2}$.

variability seen in real-world DSDs (section 5). These experiments offer insight into which assumptions made in precipitation retrieval algorithms are most consequential, what types of observations are the most important for reducing uncertainty, and how future satellite missions could be constructed to reduce uncertainties in the estimation of warm rain.

2. Data sources and models

a. OceanRAIN

The OceanRAIN project seeks to mitigate some of the challenges historically faced by in situ measurements of oceanic precipitation with the use of high-quality ODM470 optical disdrometers (Grossklaus et al. 1998) placed on board research vessels operating in remote areas. The disdrometers are manufactured by Eigenbrodt GmbH & Co. KG in Königsmoor, Germany, and measure precipitation occurrence, intensity, accumulation, phase, DSD, and ancillary meteorological data at 1-min intervals. The ODM470 is able to quickly and automatically adjust to changing wind conditions to keep the measuring volume perpendicular to the instantaneous wind direction. A detailed description of the instrument can be found in Klepp (2015). Disdrometer calibration is performed before and after shipboard operations and comparisons with a reference rain gauge (ANS410) in light-wind conditions yield accumulation differences on the order of 2% (Klepp 2015). The ODM470 has been used in several studies to evaluate satellite data and reanalysis products (Klepp et al. 2010; Bumke et al. 2016; Burdanowitz et al. 2018; Protat et al. 2019a).

TABLE 2. Passive microwave frequencies and measurement uncertainties for the three theoretical satellite architectures that are considered in this study.

	T_B frequencies (GHz)	NEDT (K)
Satellite A	94.0	4.0
Satellite B	10.6, 18.7, 23, 37, 89, 166, 183 ± 3, and 183 ± 7	0.77, 0.6, 0.51, 0.41, 0.31, 0.65, 0.56, and 0.47
Satellite C	13.6, 35.5, and 94.0	1.0, 1.0, and 1.0

We utilize OceanRAIN-M, version 1.0 (V1.0), data in this study. Raw drop counts from a 1-min collection period are converted into number concentrations, and particles are grouped into 128 logarithmically spaced bins ranging in size from 0.0375 to 22 mm. Bins 1–12 (up to 0.36 mm) are set to number concentrations of zero in the OceanRAIN-M V1.0 files because these bins can be contaminated by vibrations from the ship (Klepp et al. 2018). We found that a significant number of observations (20%–70%) also had zero values in size bins 13–17 (up to 0.54 mm), suggesting that the data from these bins is not fully reliable. Thus, we disregard these bins as well and only rain drops 0.55 mm in size or larger are included. Drizzle drops can be much smaller than this size (Wood 2005), which is why we also run experiments on data from a 2DVD disdrometer that is more sensitive to small drops (see section 2b). For calculating base-case uncertainties where DSD representation errors are disregarded, we assume that the DSD can be perfectly described by a three-parameter normalized gamma (NG) distribution of the following form (Testud et al. 2001):

$$N_D = N_w f(\mu)\left(\frac{D}{D_m}\right)^\mu \exp\left[-(4 + \mu)\frac{D}{D_m}\right], \quad (1)$$

where

$$f(\mu) = \frac{6(4 + \mu)^{4+\mu}}{4^4\Gamma(4 + \mu)}, \quad (2)$$

N_D is the number concentration (m^{-3} mm^{-1}) for drops of diameter D, N_w is the normalized intercept parameter, μ is the "shape parameter," D_m is the mass spectrum mean diameter, and $\Gamma()$ is the gamma function. The OceanRAIN-M V1.0 files contain values for D_m, N_w, and μ for each raining DSD. These parameters are fitted to the binned observations using the technique outlined in Testud et al. (2001) and Bringi et al. (2002). To calculate the rain rate from a given DSD, one must assume a relationship between drop size and fall speed. The OceanRAIN dataset does this according to the parameterization given by Atlas and Ulbrich (1974). For consistency, we use this same parameterization to calculate all rain rates considered in this study.

We use only observations marked as rain definite according to the OceanRAIN precipitation phase distinction algorithm (Burdanowitz et al. 2016), a regression method
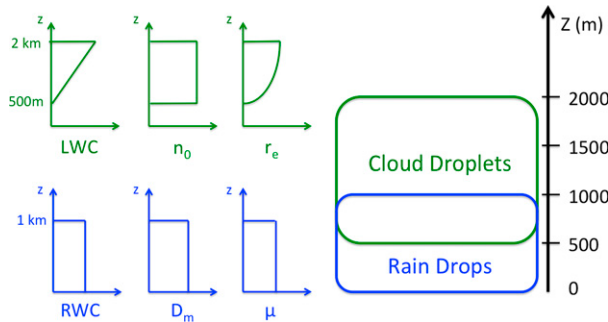
FIG. 2. Schematic of the cloud and rain profiles used in our experiments. The axes of the left qualitatively show the vertical profiles of relevant cloud DSD parameters (top; green) and rain DSD parameters (bottom; blue).

based on Koistinen and Saltikoff (1998) with the predictors of temperature, relative humidity, and 99th percentile of particle size distribution. We also screen to only include observations with 50 or more drops spread across at least 10 size bins. This results in a total of 69 677 raining minutes of data. Figure 1 shows the spatial distribution of the observations, indicating

that many of the observations occurred in previously under sampled areas including the Southern and Arctic Oceans.

b. ARM eastern North Atlantic disdrometer data

Because of the unreliable OceanRAIN data for drops smaller than 0.55 mm, we also make use of DSDs observed at the Atmospheric Radiation Measurement (ARM) Eastern North Atlantic (ENA) atmospheric observatory located on Graciosa Island in the Azores. Because the ENA site is located far from continental landmasses, we expect the observed DSDs to be characteristic of the oceanic DSDs that are of interest to this study. In addition, this region of the world is characterized by marine stratocumulus clouds, which are significant producers of warm rain (Mülmenstädt et al. 2015; Nuijens et al. 2017; Nelson and L'Ecuyer 2018). We use 1 year (1 January–31 December 2019) of data from the two-dimensional video disdrometer (2DVD) located at the site, covering drop sizes ranging from 0.1 to 10 mm in diameter (Bartholomew 2020). Giangrande et al. (2019) examined data from the same site and found that the 2DVD was better than the collocated PARS disdrometer for measuring light rain. As with the OceanRAIN data, the DSDs are averaged over a 1-min
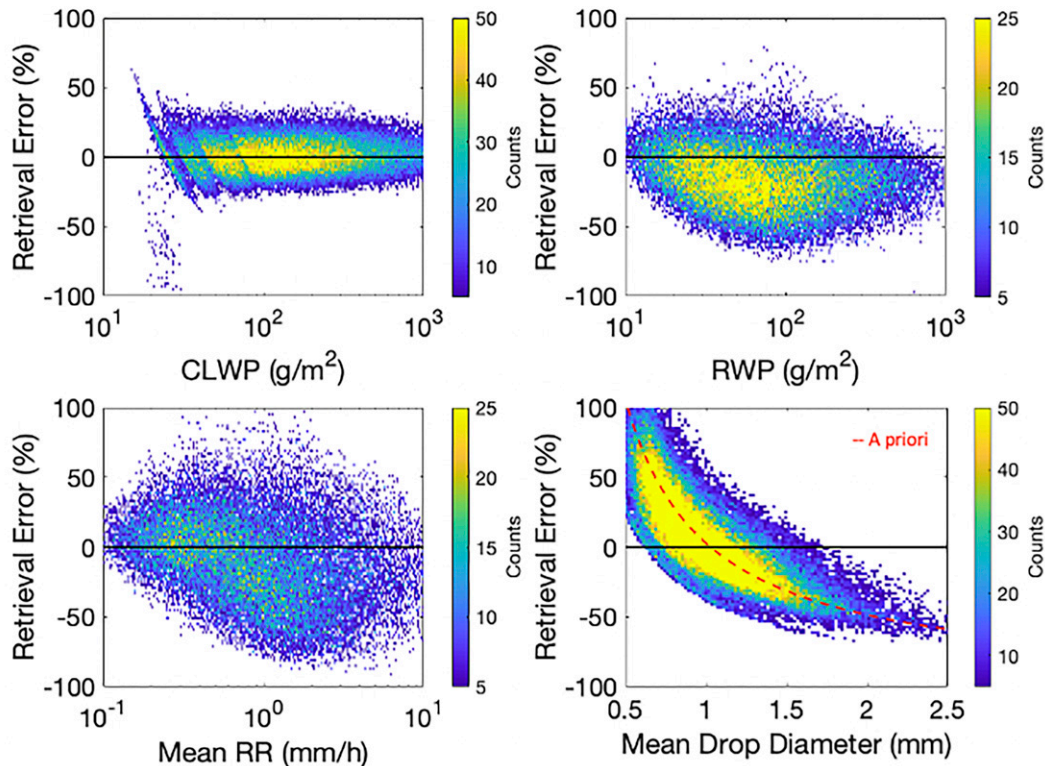

FIG. 3. Density plots of retrieved error in (top left) CLWP, (top right) RWP, (bottom left) column-averaged RR, and (bottom right) column-averaged D_m compared with the true value that was used to make the underlying simulated satellite observations for satellite architecture A. This experiment considers only sensor noise and detection limits as a source of uncertainty. The red dashed line shows the error in D_m that would be incurred if the a priori assumption were used.

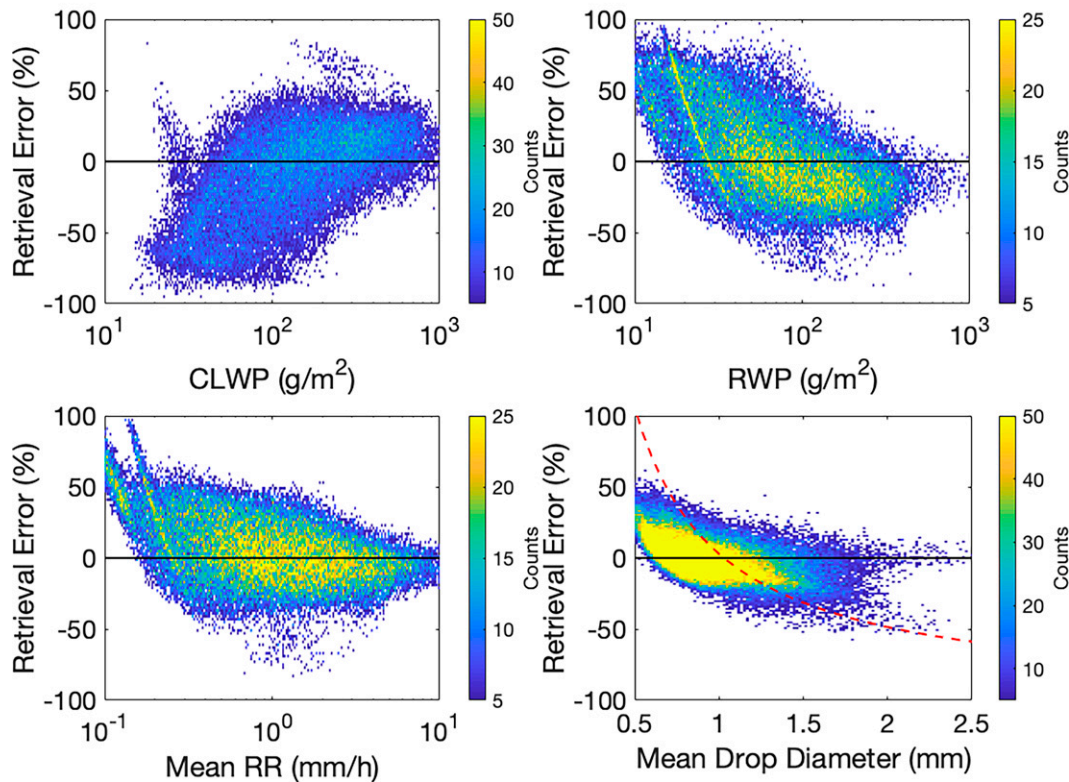## Sensor Uncertainties, Satellite B

FIG. 4. As in Fig. 3, but for satellite B.

observation window and we only use rain definite observations with more than 50 individual drops measured.

c. Radiative transfer models

In our experiments, we simulate passive microwave (PMW) brightness temperatures T_B, radar reflectivities Z, and radar two-way path-integrated attenuation (PIA). Simulated T_B are computed using the monochromatic radiative transfer model (MonoRTM; Clough et al. 2005) in combination with the FASTEM6 sea surface emissivity model (Kazumori and English 2015). For calculating the absorption and scattering of upwelling microwave radiation due to hydrometeors, spherical cloud and rain drops are assumed and Mie theory (Mie 1908) is used. Simulated Z and PIA come from the Quick-Beam radar simulator (Haynes et al. 2007). For simplicity, and because of our focus on light rain rates, multiple scattering is ignored. Another important source of error in satellite retrievals is partial beamfilling (e.g., Graves 1993). This potential source of retrieval bias is ignored in our experiments but has been studied by several other authors (e.g., Durden et al. 1998; Zhang et al. 2004; Hilburn and Wentz 2008; Tokay and Bashor 2010). An additional real-world complication that is not addressed in this study is radar surface clutter. GPM radar returns below about 1000–1500 m (depending on swath position) have too much noise to accurately detect precipitation (Kidd et al. 2021), while *CloudSat* is blind to precipitation below

about 750 m above the surface (Tanelli et al. 2008). We have ignored these important sources of retrieval error in order to focus on DSD-related uncertainties. However, many of them will be addressed in Schulte et al. (2022, hereinafter Part II, manuscript submitted to *J. Appl. Meteor. Climatol.*).

d. Ancillary assumptions

It is necessary to make many assumptions about the atmospheric column when simulating observations from the various satellite architectures. The atmospheric profiles of temperature, water vapor, and pressure are interpolated from the *U.S. Standard Atmosphere 1976* (Minzner 1977). We nominally choose a wind speed of 10.0 m s^{-1}, a sea surface salinity of 35 parts per thousand, and a sea surface temperature (SST) of 285 K. Our experiments are not especially sensitive to the choice of these profiles and surface values (assuming that corresponding changes are made to the assumptions in the retrieval algorithm). In real life, surface wind speeds and profiles of temperature and water vapor can be obtained from nearby or even coincident satellite soundings. We chose to use the same atmospheric profiles for each disdrometer observation in order to simplify the experimental methods and data sourcing required. We do, however, estimate the impact that uncertainties in these ancillary assumptions will have on final retrieved rain rates (see section 4b). We do this by perturbing the variables of temperature, water vapor mixing ratio,
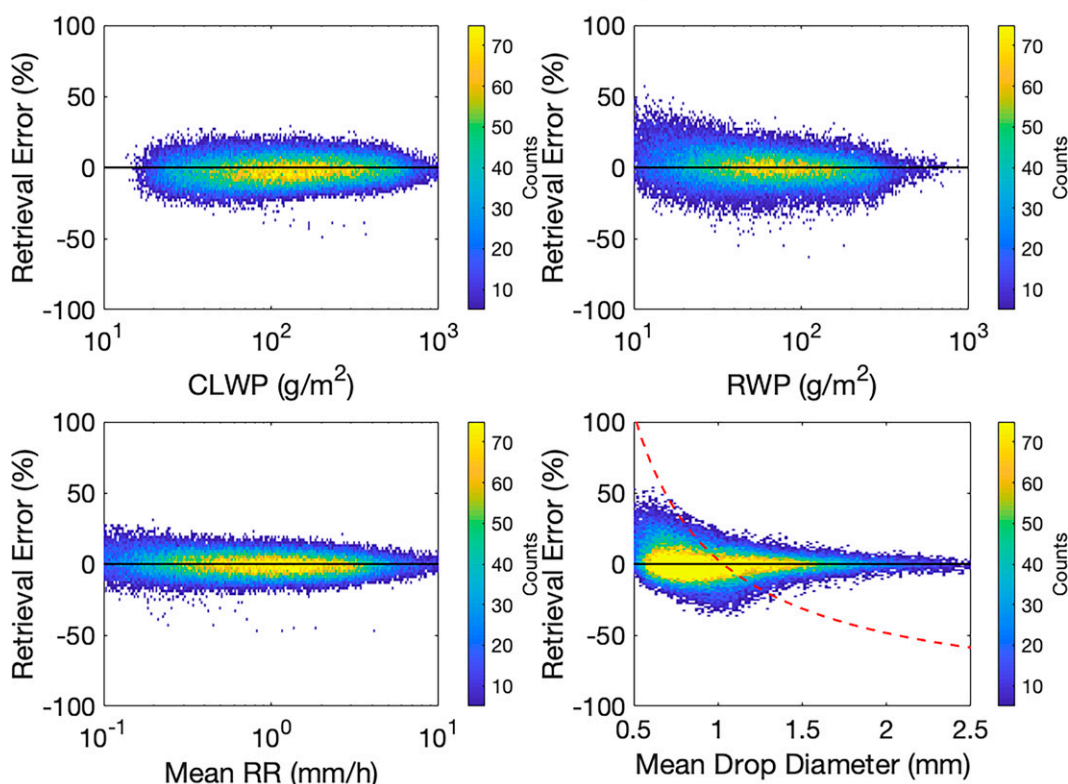
FIG. 5. As in Fig. 3, but for satellite C.

SST, surface wind speed, and cloud droplet column-averaged effective radius when simulating satellite observations. In creating the perturbations, we sample from a normal distribution centered at zero with a standard deviation of 1.0 K for temperature (including SST), 3.0 m s^{-1} for surface wind speed, 2.0 μm for cloud droplet effective radius, and 10% of the *U.S. Standard Atmosphere 1976* value at each vertical level for water vapor mixing ratio.

3. Methods

a. Simulation of satellite measurements

We consider three different theoretical satellite architectures in our experiments. The first (satellite A) is similar to *CloudSat*, with a 94-GHz nadir-viewing radar that directly gives Z at each range gate and from which a PIA and a (noisy) T_B can be derived (Lebsock and Suzuki 2016; Mace et al. 2016). The second (satellite B) is similar to the GPM core satellite, with a dual-frequency radar operating at 13.6 and 35.5 GHz (Ku and Ka band, respectively) and a PMW radiometer operating at the same frequencies as the GPM Microwave Imager (GMI; Hou et al. 2014). We consider the radar and the radiometer to have the same footprint and to make simultaneous observations of the same spot, to compare the architectures on the basis of the information content that each type of measurement can provide, without introducing

footprint differences. The third satellite, satellite C, has a triple-frequency radar that combines the W-band frequency of satellite A with the Ka- and Ku-band frequencies of satellite C. We assume that T_B can also be estimated at each of these frequencies at the same footprint of the radar, with reduced noise relative to satellite A. We also assume a heightened detection sensitivity of the radar relative to satellites A and B. Satellite C is meant to represent what might be possible with the next generation of precipitation satellites, such as that proposed by NASA's Aerosol, Cloud, Convection, and Precipitation (ACCP) study (National Academies of Science Engineering and Medicine 2018). See Tables 1 and 2 for a breakdown of the type of measurements simulated for each theoretical satellite architecture along with the assumed measurement uncertainties and sensitivities. For all radars, we assume a vertical resolution of 250 m, because this is the same vertical resolution obtained from GPM for matched Ku- and Ka-band footprints and is very close to the *CloudSat* vertical resolution of 240 m.

Since the DSD measurements contain information only at the surface it is necessary to artificially create vertical structure above. We assume that the raining column extends uniformly from the surface to a height of 1 km, and that cloud water is present from 500 to 2000 m. The amount of cloud water in each vertical level is assumed to increase linearly, as would be expected if the cloud droplets were growing adiabatically as
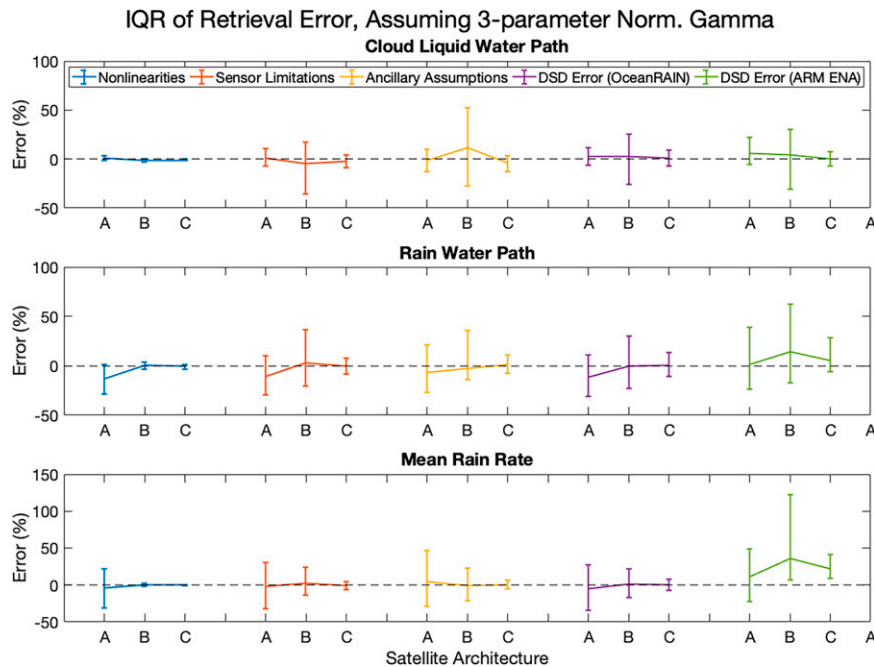
FIG. 6. Each bar shows the IQR, i.e., the 25th, 50th, and 75th percentile of retrieval errors, in (top) CLWP, (middle) RWP, or (bottom) column-averaged RR, for a given experiment and satellite architecture. The satellite is indicated by the letter on the *x* axis. The experiment being considered is indicated by the color of the bars. The blue bars are for fundamental nonlinearities only, the red bars add sensor uncertainties and detection limits, and the yellow bars add uncertainties in the ancillary assumptions. The purple bars are for the experiments with binned OceanRAIN DSDs, and the green bars are the experiments with binned ARM DSDs.

they ascended through a layer of saturated air (e.g., Miller et al. 2016). For the size of the cloud droplets, we assume an inverse exponential size distribution at each level:

$$n(d) = n_0 e^{-\lambda d}. \tag{3}$$

Here n_0 is the intercept parameter and λ is the slope parameter, which can be related to the effective radius r_e by

$$\lambda = 3/(2r_e). \tag{4}$$

We construct the cloud water distribution such that n_0 stays the same throughout the cloud but r_e increases toward cloud top, with the additional constraint that the average r_e for the whole cloud is 11 μm. A coordinated intercomparison of satellite cloud data records (Stubenrauch et al. 2013) found a consistent peak in cloud droplet effective radius at this value, and it is also broadly in line with other studies such as Witte et al. (2018) and Sinclair et al. (2021). Figure 2 shows qualitatively what the vertical profile of cloud and rain looks like. The scenario is highly idealized but serves our purposes of evaluating DSD-related retrieval uncertainties.

b. Optimal estimation retrieval algorithm

From the simulated satellite observations, we use an optimal estimation (OE) retrieval algorithm to try to retrieve the cloud liquid water path and the DSD parameters necessary to calculate the cloud-base rain rate (RR). The method is based on Bayes's theorem,

$$P(\mathbf{x}|\mathbf{y}) = \frac{P(\mathbf{y}|\mathbf{x})P(\mathbf{x})}{P(\mathbf{y})}, \tag{5}$$

where $\mathbf{y}$ is the measurement vector containing all of the observations being considered and $\mathbf{x}$ is the state vector consisting of the hydrometeor properties being retrieved.

According to Eq. (5), to find the value of $\mathbf{x}$ for which the posterior probability $P(\mathbf{x}|\mathbf{y})$ is maximized, one should search for the state vector that maximizes the product of the a priori probability of that state, $P(\mathbf{x})$, with the probability of measuring the set of observations $\mathbf{y}$ if $\mathbf{x}$ was indeed the proper state vector, $P(\mathbf{y}|\mathbf{x})$. As demonstrated by Rodgers (2000), if one assumes Gaussian errors, maximizing $P(\mathbf{x}|\mathbf{y})$ is equivalent to minimizing the following cost function Φ:

$$\Phi = (\mathbf{x} - \mathbf{x}_a)^{\mathrm{T}} \mathbf{S}_a^{-1} (\mathbf{x} - \mathbf{x}_a) + [\mathbf{y} - f(\mathbf{x}, \mathbf{b})]^{\mathrm{T}} \mathbf{S}_{\mathbf{y}}^{-1} [\mathbf{y} - f(\mathbf{x}, \mathbf{b})]. \tag{6}$$

Here, f is a forward model based on radiative transfer theory that is able to simulate all of the observations that make up the observation vector. The vector $\mathbf{b}$ contains additional ancillary
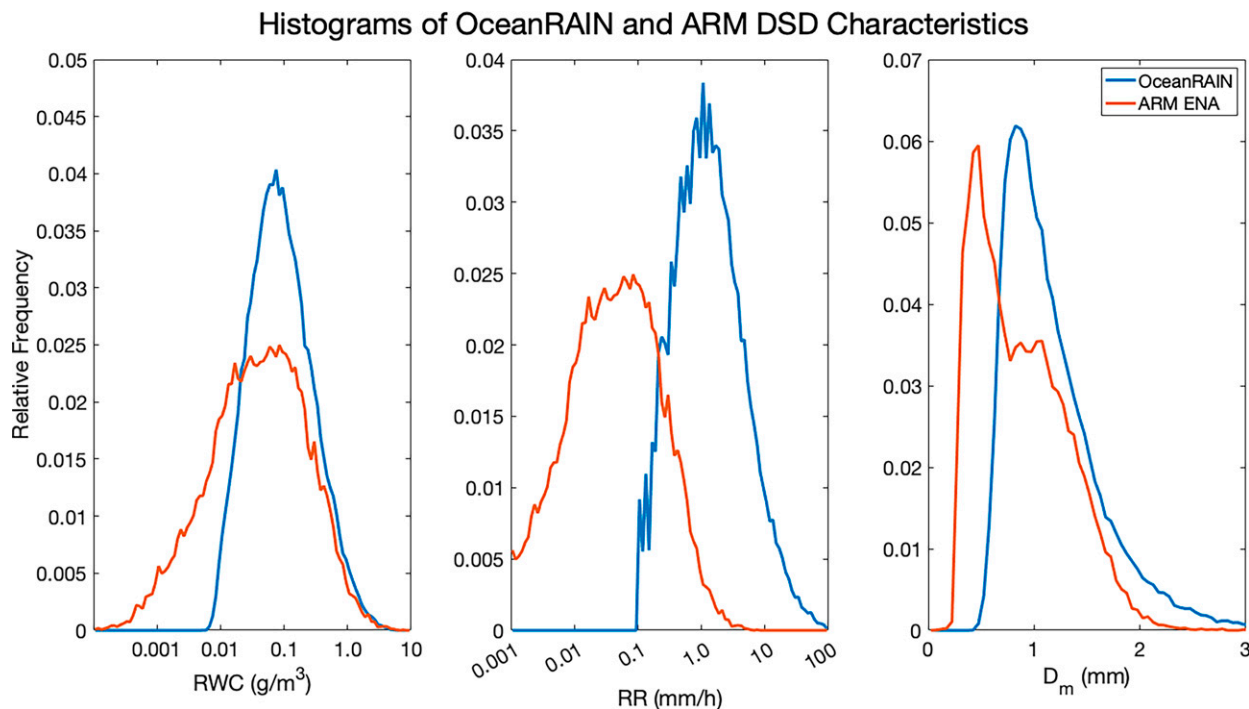
FIG. 7. Histograms showing the (left) RWC, (center) RR, and (right) D_m distributions for the OceanRAIN and ARM ENA disdrometer datasets.

information, besides those parameters that make up **x** and for which one directly solves, that is required by the forward model to simulate the full observation vector.

The first term of the cost function weights departures of a potential state vector **x** from the a priori state vector $\mathbf{x}_a$ by the assumed errors in the a priori state, as described by the a priori covariance matrix $\mathbf{S}_a$. Similarly, the second term weights the difference between observations **y** and forward-model output $f(\mathbf{x}, \mathbf{b})$ by a second error covariance matrix, the $\mathbf{S_y}$ matrix, which describes the uncertainties in both the observations and the forward model. Using the Gauss–Newton method, we iteratively solve for the value of **x** at which the gradient of the cost function, $\nabla_{\mathbf{x}}\Phi$, is equal to zero. For more background on the OE algorithm, see Schulte and Kummerow (2019) and Schulte et al. (2020), because the algorithm is based on the same mathematical and radiative transfer backbone as the PMW inversion algorithm [Colorado State University (CSU) 1DVAR] used in those studies. This algorithm differs from the CSU 1DVAR in that it retrieves a different set of parameters and is built to incorporate radar observations (both Z and PIA) into the observation vector in addition to T_B.

The state vector contains four parameters: the vertically integrated cloud liquid water path (CLWP), the rainwater content (RWC) of the DSD, the mass-weighted mean diameter D_m of the DSD, and the normalized gamma shape parameter μ of the DSD. CLWP, RWC, and D_m are retrieved in logarithmic space because their underlying distributions are not normally distributed but are much closer to a lognormal distribution. RWC, D_m, and μ are all functions of height in reality, but we assume that

they are constant throughout the raining column and so can be thought of as column averages. The size of the observation vector depends on the satellite architecture used as well as the atmospheric profile being considered. It is equal to the number of PMW channels in the architecture, plus the number of PIA frequencies, plus the number of valid radar observations. A valid radar observation, for these purposes, is one for which the reflectivity exceeds the minimum detectable signal for that satellite and radar frequency.

The forward model $f(\mathbf{x}, \mathbf{b})$ uses the same radiative transfer models (i.e., QuickBeam and MonoRTM, introduced in section 2c) that are used for creating simulated satellite observations. Because the OE forward model is based on the same code (i.e., we are assuming no radiative transfer model error), the forward-model errors are underestimated relative to what would be expected in real-world retrievals. Eliminating this forward-model error allows us to isolate other sources of error, such as DSD representation error, that are the focus of our study.

c. Error covariance matrices

The $\mathbf{S}_a$ and $\mathbf{S_y}$ matrices are constructed based on the statistics of the related error distributions. For example, when using the OceanRAIN disdrometer data, the $\mathbf{S}_a$ matrix contains the variance of $\log_{10}(\text{LWP})$, $\log_{10}(\text{RWC})$, $\log_{10}(D_m)$, and μ found in the OceanRAIN dataset on the diagonal, and the covariances between the OceanRAIN parameters make up the off-diagonal elements. The $\mathbf{S_y}$ matrix is meant to account for both forward-model and sensor uncertainties, although in most cases the forward-model uncertainty dominates. The forward-
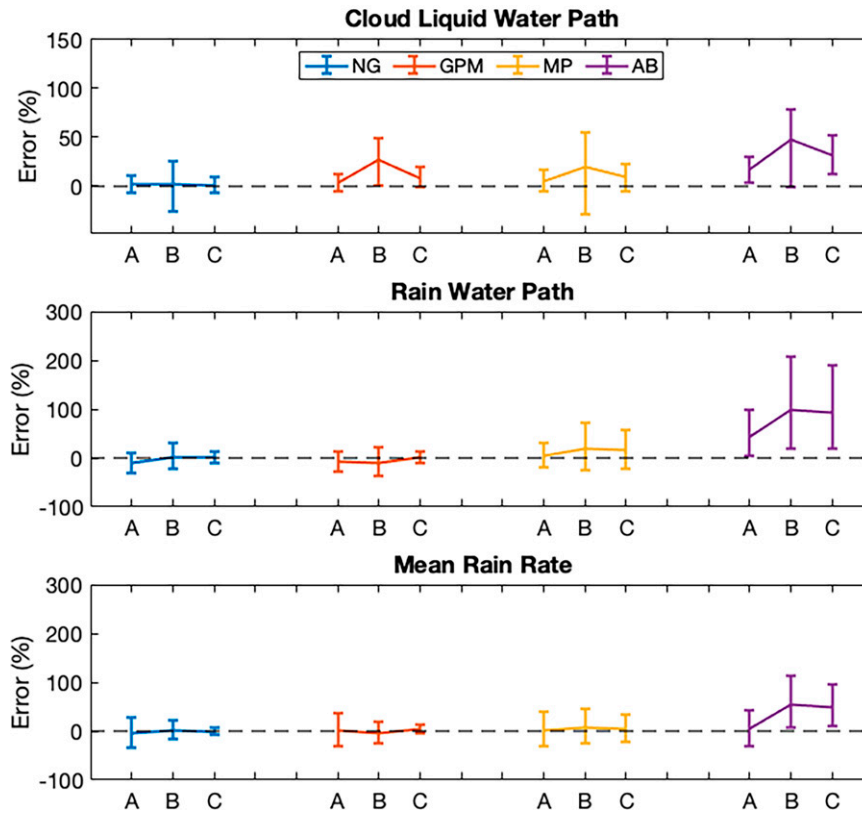
IQR of Retrieval Error for Various Assumed DSDs

FIG. 8. IQR of retrieval errors for a given satellite architecture, using a forward model in the OE algorithm that assumes a three-parameter NG DSD (blue), a two-parameter NG distribution (red), an MP distribution (yellow), or an AB distribution (purple).

model uncertainties are estimated by comparing the simulated observations produced by the simplified forward model with simulations in which the various assumptions of the forward model are relaxed (in the real world, one could compare with true observations). Then the sensor uncertainties are added to create the full S_y matrix. See Schulte and Kummerow (2019) for more details about the construction of covariance matrices.

One disadvantage of an OE algorithm is that, even if there were no observation or forward-model uncertainties, the algorithm would only be guaranteed to converge to the proper solution if the problem were linear. Precipitation retrievals are known to be not entirely linear (e.g., Stephens and Kummerow 2007). Other retrieval techniques exist that are less subject to nonlinearities, such as neural network based algorithms (Beusch et al. 2018; Tang et al. 2018; Chen et al. 2019) or Markov chain Monte Carlo (MCMC) approaches (Posselt et al. 2017; Xu et al. 2019). Still, the OE approach provides several benefits. The algorithm is based on physical radiative transfer models rather than statistical correlations, retrieval performance can be compared across different satellite architectures in a consistent and simple fashion, and the method provides a posteriori error estimates that can be traced directly to the underlying uncertainties and the physics of the problem. In most cases, as explored further in section 4, the fundamental uncertainties due to the

nonlinearities of rainfall retrieval are much smaller than the retrieval errors that result from the other sources of uncertainty that we consider.

4. Base-case uncertainties

a. Uncertainties due to sensor noise, detection limits, and nonlinearities

In this first experiment, we quantify how sensor limitations affect retrieval errors and uncertainties. We use the OceanRAIN NG-fitted DSDs to create simulated satellite observations. Because the disdrometer observations do not tell us anything about how much cloud water is in the column, we nominally set the column-integrated CLWP so that it is equal to twice the column-integrated rainwater path [note that the OE algorithm is unaware of this assumed relationship and is free to converge to any CLWP value regardless of rainwater path (RWP)]. Random Gaussian noise is added to the synthetic observations to simulate the physical limitations of the satellite instruments, using the measurement uncertainty values given in Tables 1 and 2. Then, after adding the measurement noise, if a certain radar measurement has a value below the detection limits given in Table 1, the measurement is set to have no radar

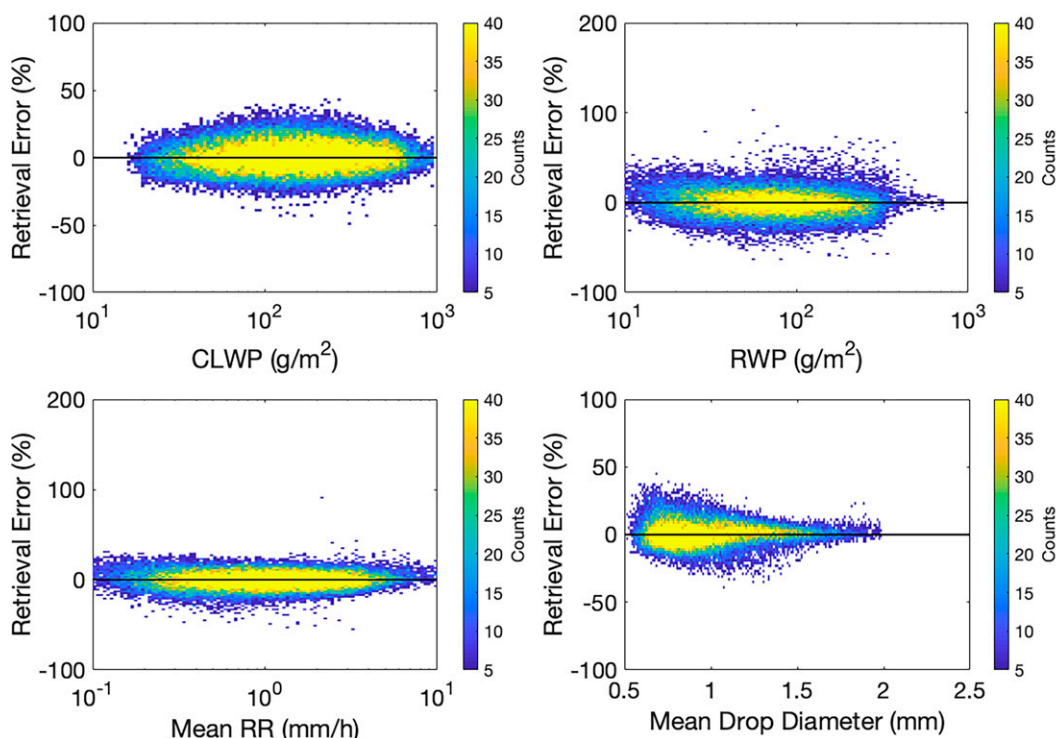## Satellite C Retrieval Errors Assuming Normalized Gamma DSD

FIG. 9. As in Fig. 5, but using OceanRAIN binned DSDs to simulate observations and assuming a three-parameter NG DSD model in the OE.

echo. This has the effect of getting rid of about 6% of cloud-only radar observations for satellite A and all of the cloud-only and about 8% of the rain observations for satellite B and reducing satellite C to only a single (W band) frequency for cloud-only observations. The algorithm then retrieves the four elements of the state vector, from which the RR is calculated.

Figures 3–5 show the results of this experiment. Starting with satellite A, we see that, even with only W-band observations, the CLWP is well constrained. The retrieval error is very close to 0% throughout the whole range of CLWP, with an overall retrieval bias (defined as the median retrieval error) of 1.2% and an interquartile range (IQR) of errors of 18.2%. The IQR is the difference between the 25th-percentile and 75th-percentile errors. On the other hand, the RWP is negatively (low) biased (−11.0%) and the column-averaged RR also slightly negatively (low) biased (−1.6%), although the RR bias mostly comes from the higher rain-rate cases. Both parameters show considerable spread. Unsurprisingly, given that it has only a single radar frequency, satellite A shows little skill in retrieving D_m. The retrieved D_m values are clustered very closely around the a priori value (represented by the red dotted line), resulting in overestimation at low D_m and underestimation at high D_m.

Satellite B demonstrates more skill at retrieving D_m and, to a lesser extent, RWP and RR. However, CLWP is not well constrained, with a bias of −4.8% and an IQR of 53.2%. Since cloud drops as well as small rain drops fall below the radar detection limits, the architecture struggles to differentiate cloud

drops from drizzle drops. This underscores the importance of the W-band radar for cloud/rain partitioning. Satellite C, on the other hand, does a remarkably good job of constraining all of the retrieved quantities of interest. There is less bias in the retrieved CLWC, RWP, and RR, and the IQRs are relatively small at 13.2%, 16.6%, and 11.2%, respectively.

We also ran an experiment in which we input simulated satellite observations directly into the retrieval algorithm, without adding sensor noise or detection limits. Thus, the only limitations faced by the retrieval in this case were the fundamental nonlinearities of the inversion problem. Nonlinearities can potentially create challenges for an OE retrieval by causing the algorithm to converge to a local, rather than absolute, minimum of the cost function. The IQRs from these experiments can be seen in Fig. 6. From these results it is clear that the nonlinearities of the problem should not be a major concern, except perhaps for the case of retrieving RR and RWP from satellite A, for which there is a slight negative bias in the retrieved values.

b. Ancillary assumption uncertainties

In another experiment, we add random noise (see section 2d for details) to the atmospheric profiles before simulating satellite observations, in order to estimate the uncertainty that is introduced into real-world satellite precipitation retrievals by ancillary assumptions. Once the satellite observations have been simulated, we add measurement noise, eliminate observations below detection limits, and run the OE algorithm with our

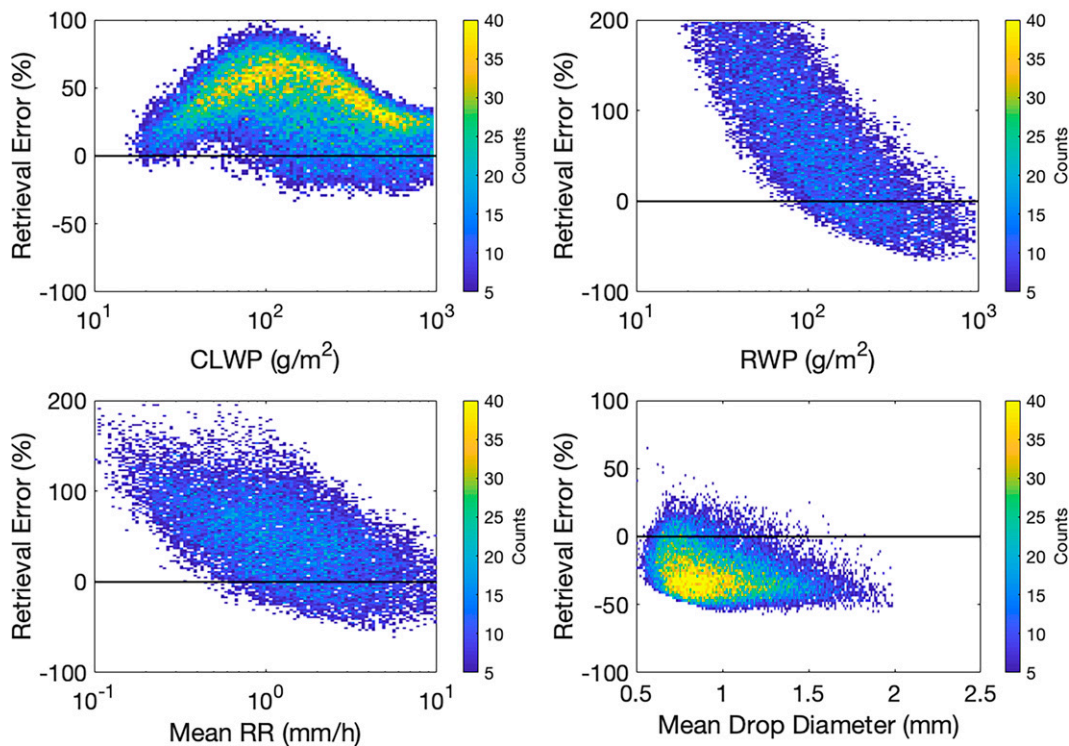## Satellite C Retrieval Errors Assuming Abel & Boutle DSD

FIG. 10. As in Fig. 5, but using OceanRAIN binned DSDs to simulate observations and assuming the single-parameter normalized DSD model of Abel and Boutle (2012) in the OE.

original assumptions about the atmospheric profile intact. The main effect of introducing these uncertainties is, as expected, an increase in the IQR of retrieval errors for all satellite architectures. This increase is perhaps most pronounced for the retrieval of CLWP from satellite B, for which the IQR increases from 53.2% to 80.2%. Most of this architecture's CLWP information comes from T_B, so errors in the assumed temperature and water vapor profiles cause T_B differences that translate into increased retrieved CLWP errors. Otherwise, the error biases in this experiment stay close to zero but with a modestly larger spread for most parameters of interest.

5. DSD-related uncertainties

a. Experiments with binned DSDs

In these next series of experiments, we explore how DSD assumptions affect retrieval uncertainties and biases. First, we simulate satellite observations using the raw drop concentrations for each size bin, instead of using the fitted NG DSD parameters from OceanRAIN. As discussed in section 2, we use only rain drops larger than 0.55 mm in diameter. As in the base case, we add sensor noise and eliminate observations below detection limits, and then use these simulated satellite observations to retrieve the cloud and rain parameters, assuming a three-parameter NG rain DSD. To be consistent, we adjust the forward model in the OE algorithm so that it

also ignores rain drops smaller than 0.55 mm in size. The resulting spread of retrieval errors can be seen in Fig. 6. Relative to the base case, the spread is slightly larger but not by much. This indicates that the NG model can capture the real-world variability of drop spectra (at least on the larger end of the size range) and is appropriate for use in retrieval algorithms, confirming the findings of previous studies (e.g., Testud et al. 2001; Bringi et al. 2002; Adirosi et al. 2014). Most of the biases are near zero, with the exception being a slight underestimation of RWP and RR for satellite A, which is also present in the base-case experiment. Since satellite A only has W-band observations, and W-band Z tend to saturate at moderate rain rates, it would make sense that this architecture could underestimate rain in heavier precipitation.

To investigate the effect of including smaller drops from 0.1 to 0.55 mm, we repeat the same experiment but use binned DSDs from the ARM ENA site instead of OceanRAIN observations. These observations differ from the OceanRAIN observations not only because of their inclusion of small drops but also because the frequency of occurrence of very light rain and drizzle is much larger in this dataset than in the OceanRAIN dataset, as can be seen in Fig. 7. This is consistent with the findings of Giangrande et al. (2019) that the ENA site receives a significant portion of its precipitation from marine low clouds and that median raindrop sizes at the site are smaller than what is typically seen at other locations
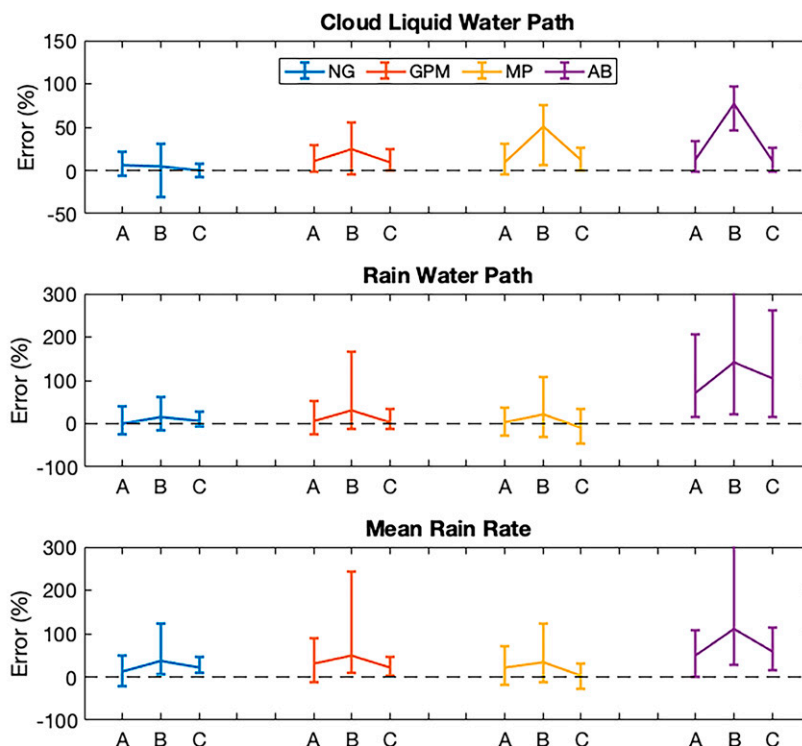
FIG. 11. As in Fig. 8, but using ARM ENA disdrometer data for the underlying rain drop distributions instead of OceanRAIN.

around the globe. The resulting retrieval errors are larger using the ARM DSDs than the OceanRAIN DSDs, especially for RWP and RR (refer again to Fig. 6). There is also a bit of a retrieval bias. While the retrieved RWP is biased only moderately high, the retrieved RR is biased 11.6% to 36.3% high, depending on the satellite. Thus, while the assumption of a NG DSD works well for the retrieval of light to moderate rain from OceanRAIN, it might not be as appropriate for the retrieval of drizzle rates. Others have found that the generalized gamma model (Thurai and Bringi 2018), which includes a second shape parameter, can more accurately represent the drizzle mode of the DSD, although retrieval gains would only be realized if satellite measurements were able to accurately detect changes to this parameter.

b. Impacts of assuming alternative DSD models

The three free parameters of the normalized gamma DSD model allow for most realistic DSDs to be reasonably fit by a NG distribution. Most precipitation retrieval algorithms, however, do not retrieve three DSD parameters. If only one or two radar frequencies are employed, there is a reasonable argument to be made that one should only retrieve one or two DSD parameters, as otherwise the inversion could be under constrained. Still, using a DSD with fewer free parameters will make it harder for the forward model used in the retrieval to mimic the true underlying DSD, leading to greater uncertainty

in retrieved rain rates. In this section we attempt to quantify the uncertainties and biases resulting from assuming three alternative DSD models in our OE algorithm instead of a three-parameter NG.

The first model we test is a two-parameter NG model, where we retrieve column-averaged RWC and D_m as before but the shape parameter μ is constrained to always be equal to 3, as in the GPM dual-frequency radar precipitation retrieval (Seto and Iguchi 2015). We also test two single-parameter models, where we only retrieve column-averaged RWC. The assumptions made in the models are then enough to uniquely determine the full drop size spectrum. The first model is that of Marshall and Palmer (1948), which was based on raindrop records on dyed filter papers from Ottawa, Canada. We use this model as a reference because it is well-known and was used in early formulations of the *CloudSat* 2C-RAIN-PROFILE algorithm (Lebsock and L'Ecuyer 2011). We also test the model of Abel and Boutle (2012), which is currently used by the 2C-RAIN-PROFILE algorithm (Lebsock 2018). Both the Marshall–Palmer (MP) and Abel and Boutle (AB) models are based on inverse exponential distributions but differ in how the shape of the distribution is related to the overall RWC of the DSD. In the AB model, the intercept parameter is related to the slope parameter by the equation

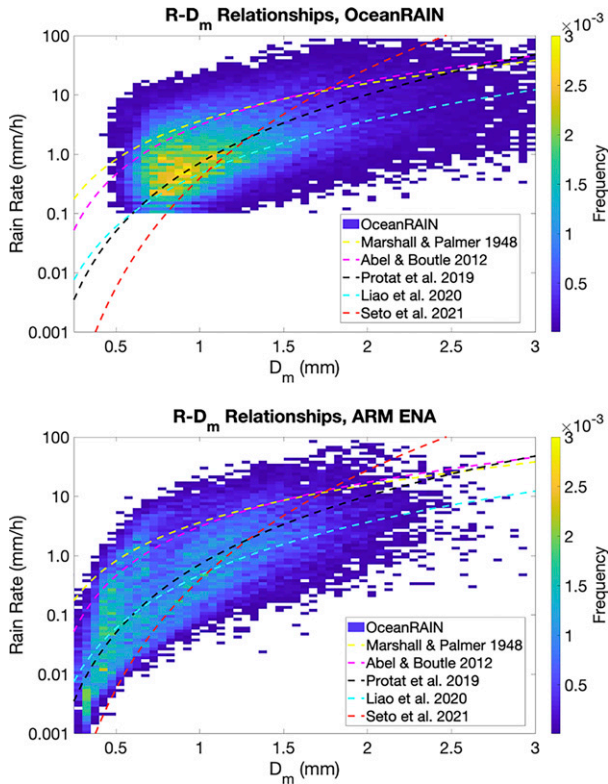$$N_0 = x_1 \lambda^{x_2}, \tag{7}$$

FIG. 12. Frequency distributions of (top) OceanRAIN and (bottom) ARM DSD observations according to their rain rate (y axis) and mass-weighted mean drop diameter (x axis). The dotted curves show the R–D_m relationships reported by several different studies (cited in the text).

where x_1 is set to 0.22 and $x_2 = 2.2$. The slope parameter λ is determined from the rain mass mixing ratio q_R by the equation

$$\lambda = \left(\frac{\pi \rho_w x_1}{\rho_{air} q_R}\right)^{1/(4-x_2)}, \tag{8}$$

where ρ_w and ρ_{air} are the densities of water and the air parcels, respectively. In the AB model, DSDs with a high RWC have a lower intercept parameter (fewer very small drops) than those with low RWCs, making up this difference with even more large drops. Under MP assumptions, all DSDs have the same intercept parameter (i.e., similar numbers of very small drops), but those with a larger RWC have more large drops.

We repeat the OceanRAIN binned DSD experiment, but this time assuming these different DSDs models in the OE forward model. Figure 8 shows the effect that assuming each of these simplified DSDs has on retrieval errors. Relative to the control run assuming a three-parameter NG, holding μ fixed does not increase the retrieval uncertainties very much. There is, however, a slight tendency to substitute cloud water for rainwater, with a high bias in retrieved CLWP and a low bias in retrieved RWP (for satellites A and B). The retrieved rain rate, on the other hand, does not show much of a bias for any of the satellite architectures.

Both single-parameter DSD models (in the yellow and purple) yield considerably more retrieval uncertainty than the two- or three-parameter NG models. In addition, they also lead to a positive bias in retrieved RWP and RR, no matter which satellite architecture is considered. This is especially true for the AB model, for which the retrieved RWP is positively (high) biased by between 42% and 94% (depending on satellite architecture), and the retrieved RR is positively (high) biased by between 5% and 55%. Figures 9 and 10 show the full retrieval error densities for satellite C assuming either the three-parameter NG model (Fig. 9) or the AB model (Fig. 10). In comparing the two figures, it is even more evident that the AB model assumption results in an overestimation of retrieved RWP and RR, especially at rain rates less than about 5 mm h^{-1}. Meanwhile, the CLWP is consistently positively (high) biased and D_m is consistently negatively (low) biased.

To test the robustness of these results, we performed the same set of experiments using the ENA binned DSDs to simulate satellite observations. In this case the errors seen in the OceanRAIN experiment are magnified even more, as shown in Fig. 11. The RR biases range from 49% to 110% for the AB experiment. From these results, it is clear that the DSD assumed in a retrieval algorithm can have a very large impact on retrieved RR. Notably, the AB DSD does not seem very appropriate for cases of light rain, which dominate the ARM ENA dataset. This could partially explain why *CloudSat* tends to retrieve more rain over the high latitudes than GPM (Behrangi and Song 2020). In both the OceanRAIN and ENA experiments, we find that assuming the AB (*CloudSat*) DSD instead of the two-parameter NG (GPM) DSD leads to retrieved RRs that are about 25%–50% higher.

We believe this overestimation from the AB and MP models stems in part from the fact that the MP and AB models assume size spectra that are too heavily concentrated toward small drops. Figure 12 plots the relationship between RR and D_m in the OceanRAIN and ARM datasets, along with the curves that result from the AB and MP models. For reference, we also include RR–D_m curves reported by Protat et al. (2019a), Liao et al. (2020), and Seto et al. (2021). Both the AB and MP models predict a much higher RR for a given D_m than what is observed in either disdrometer dataset or predicted by the other models, indicating a higher overall RWC. The Z values are most strongly affected by the largest drops in a given rain volume, because in the Rayleigh regime reflectivity scales as D^6. If the OE algorithm is assuming one of these models, the implication is that to create forward-modeled reflectivities that match what has been observed (i.e., have a similar D_m) the OE must assume a much higher overall RWC. This effect is so large that it translates into a higher RR, despite the partially compensating effect that small drops fall more slowly than large ones.

c. Latitudinal differences

As seen in Fig. 1, the OceanRAIN dataset contains observations from a wide variety of locations. The highest concentration of observations come from the Southern Ocean,
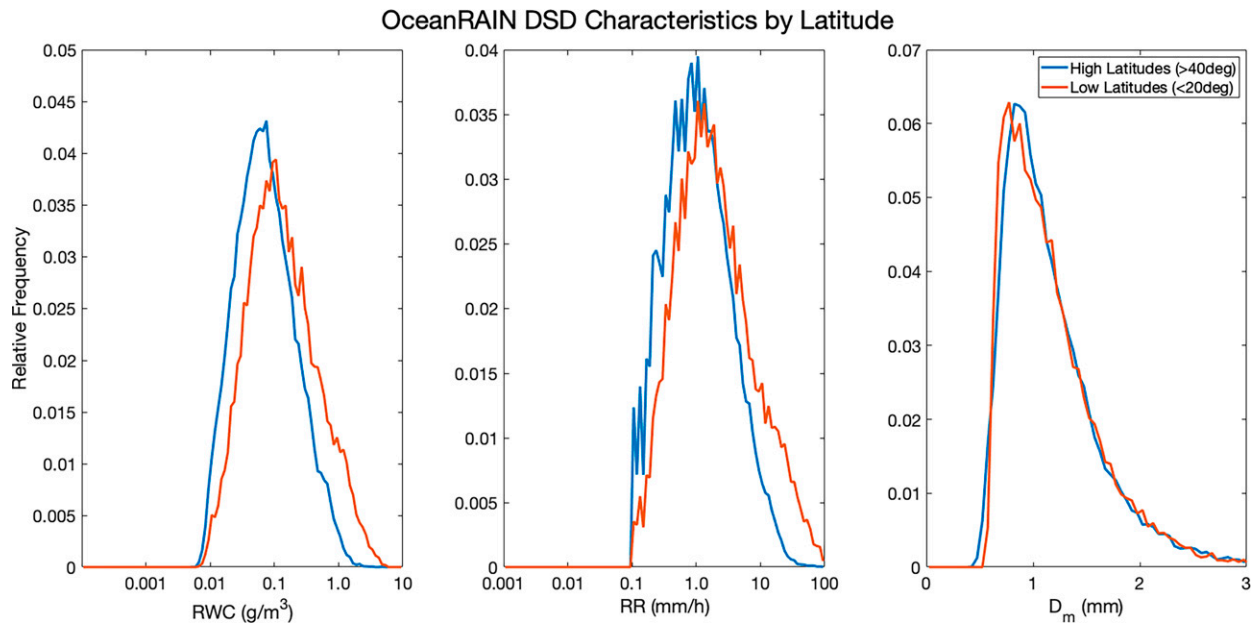
FIG. 13. Histograms comparing the (left) RWC, (center) RR, and (right) D_m distributions for the OceanRAIN disdrometer observations taken at latitudes between 20°S and 20°N (red) or at latitudes north of 40°N or south of 40°S (blue).

but a secondary maximum occurs in the tropics. Figure 13 shows comparison of OceanRAIN DSD statistics between "low latitude" observations (those taken between 20°S and 20°N) and "high latitude" observations (those south of 40°S or north of 40°N). The high-latitude DSDs tend to have lower RWCs and RRs but also have a slightly larger mean D_m; that is, the high-latitude DSDs have significantly fewer drops overall but the drops that do exist are slightly larger. This could be due to the low concentration of cloud condensation nuclei in these regions (Gras 1995; Ayers et al. 1997; Humphries et al. 2021).

To test whether tropical DSDs have different retrieval error characteristics than high-latitude DSDs, we repeated the simulated retrieval experiments using either the high- or low-latitude subset of OceanRAIN DSDs. For most of the experiments, there were only small differences between retrieval performance on each subset. An example is shown in the bottom half of Fig. 14. However, when the AB model was assumed in the retrieval algorithm, higher biases in retrieved RWP and RR were found using the high-latitude DSDs. For example, the RR bias for satellite C was only 20.7% when tropical DSDs were used but increased to 64.4% for high-latitude DSDs. This result suggests that the Abel and Boutle (2012) DSD model might be especially inappropriate for high-latitude DSDs, but that the normalized gamma model is flexible enough to handle the variability in DSD shapes observed by OceanRAIN.

6. Conclusions

There are clearly many challenges and uncertainties to address in retrieving precipitation from a satellite platform, including important ones that we have not dealt with in this

study, such as surface clutter, frozen hydrometeors, field of view heterogeneities, and vertical structures that can differ substantially from the idealized scenario assumed in this study. Many of these uncertainties will be quantified in Part II (manuscript submitted to *J. Appl. Meteor. Climatol.*) of this study. It is also likely that our use of a priori data biases the retrieval results toward the correct answer, so the uncertainties we calculate should be thought of as very much best-case values. Our results nevertheless offer important insight into the significance of DSD uncertainty when it comes to retrieving rain.

One common thread running through all of our experiments is the importance of W-band observations for differentiating cloud water from rainwater. For satellite architectures A and C, both of which include 94 GHz radars, CLWP is generally the easiest of the retrieved variables to constrain, but CLWP uncertainties increase greatly for satellite B, which has a tendency to substitute rainwater for cloud water and vice versa. This is because both cloud droplets and drizzle drops tend to have reflectivities below the Ka/Ku detection limit of 12 dBZ. It is thus very important that future satellite missions include W-band radar observations. Of the other retrieved variables, the DSD shape parameter μ is the hardest to retrieve accurately, followed by the volume-weighted mean diameter D_m. For the purposes of deriving rain rate, D_m is much more consequential.

Fundamental nonlinearities set a lower limit on the retrieval uncertainties one can expect from an optimal estimation based retrieval. For satellites B and C, these pale in comparison with the other uncertainties considered in this study, while for satellite A, which only has one radar frequency, the nonlinear nature of the inversion problem presents more of a challenge. Adding
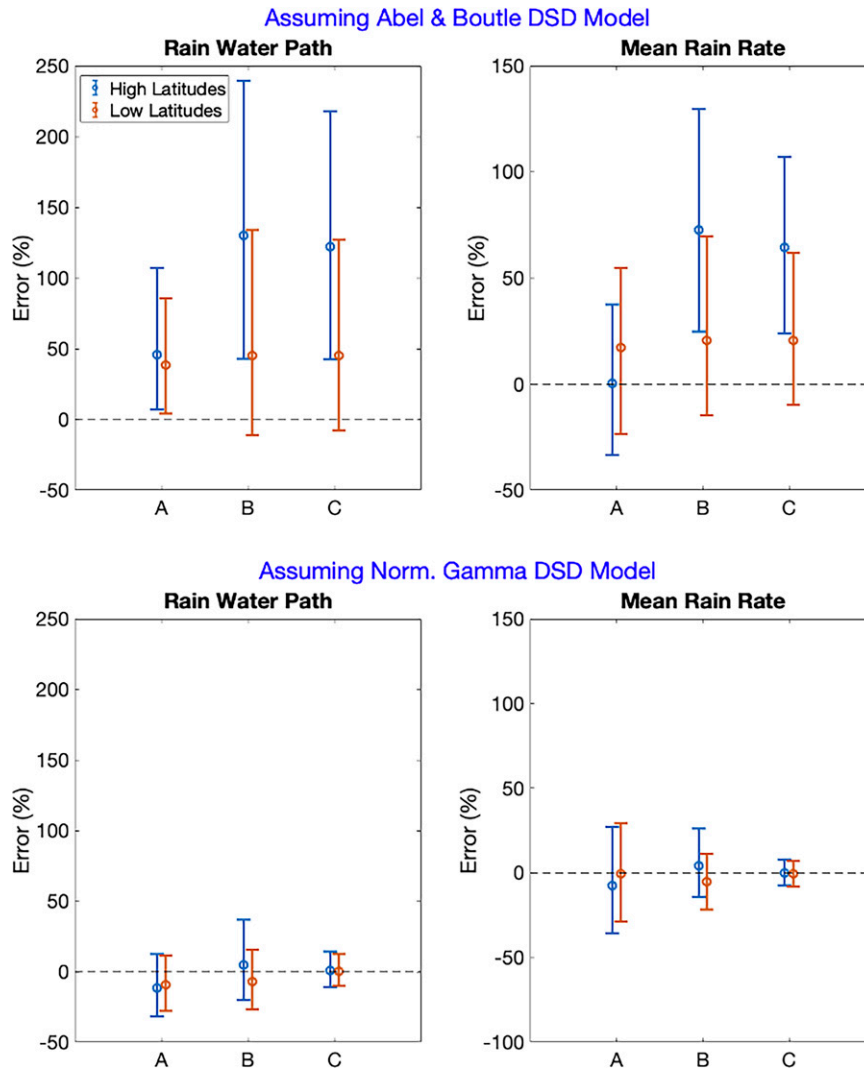
FIG. 14. IQR of retrieval errors for (left) RWP and (right) RR for each satellite architecture, assuming either the (top) single-parameter AB DSD model or (bottom) three-parameter NG DSD model in the retrieval algorithm. Blue bars correspond to "high latitude" cases (latitudes > 40°N or S), and red bars correspond to "low latitude" cases (latitudes between 20°S and 20°N).

sensor noise and detection limits increases the retrieval uncertainty but does not lead to a retrieval bias. We see a similar effect when we consider uncertainties in the ancillary assumptions about the surface and atmospheric profile that the retrieval must make in order to simulate satellite observations.

Our assumption of a three-parameter NG DSD works well for the OceanRAIN disdrometer data. However, DSDs from the ARM ENA disdrometer are not as well represented, and the NG assumption leads to a positive bias in retrieved rain rate as the retrieval algorithm tends to assume the drops are larger than they actually are. Even larger biases result when single-moment DSD parameterizations are assumed in the retrieval algorithm, including positive biases near 100% for retrieving rain rate from the ENA disdrometer data. Relative to the two-parameter NG DSD (used by some GPM algorithms),

the single-parameter AB model (used by the *CloudSat* 2C-RAIN-PROFILE algorithm) retrieves rain rates that are 25%–50% higher, depending on satellite architecture. The differences are especially large for high-latitude DSDs and for light rain. These experiments clearly show that DSD assumptions have a large impact on satellite precipitation retrievals.

Our results are focused on warm-rain uncertainties, in that our simulated satellite observations include only liquid hydrometeors. We would expect retrieval uncertainties for more complicated precipitation types to be larger because of additional nonlinearities and the difficulty in accurately modeling ice particle shapes in a forward model. An important caveat is that we cannot guarantee that the OceanRAIN and ARM surface observations used in this study resulted from warm-rain-only

precipitation processes. While ARM ENA observations come predominantly from low marine clouds (Giangrande et al. 2019), we have not attempted to exclude DSDs from deep clouds in our analysis. We also caution that we have used surface DSD observations, when in reality satellite radars cannot sense below 750 m above the surface (at best) because of surface clutter. Given these limitations, we would stop short of saying that any of the DSD models considered in this study are definitively "best" for retrieving warm rain. It is possible, for instance, that if one were looking at only warm-rain processes at 1000 m above the surface (where less evaporation of small drops has taken place), the AB model would be more appropriate. In this hypothetical, DSD assumptions would still be an important source of retrieval bias, since the operational *CloudSat* and GPM algorithms assume very different R–D_m relationships (see Fig. 12). Regardless of which one is more correct, the fact that they are so different likely explains part of why rain rates retrieved from GPM are lower than those from *CloudSat* in light rain regimes (Behrangi and Song 2020).

Our findings offer a cautionary tale for all satellite retrieval algorithms. Careful attention needs to be paid to DSD assumptions when interpreting and comparing retrieved rain rates. Simple DSD parameterizations may not be appropriate, especially for remote, high-latitude oceanic regimes. Our work shows that, when multiple radar frequencies are available (such as for architecture C in this study), retrieving two or three moments of the DSD can be greatly helpful in narrowing retrieval uncertainties because a greater variety of DSD shapes can be described by such a model. This should be an important consideration when designing the next generation of satellite precipitation missions and algorithms. For missions such as *CloudSat*, where the limited information content of a single-frequency radar makes it harder for multiple DSD moments to be retrieved, more research is needed into how DSD shapes are regime dependent and whether these dependencies could be usefully incorporated into a retrieval algorithm.

REFERENCES

Abel, S. J., and I. A. Boutle, 2012: An improved representation of the raindrop size distribution for single-moment microphysics schemes. *Quart. J. Roy. Meteor. Soc.*, **138**, 2151–2162, https://doi.org/10.1002/qj.1949.

Adirosi, E., E. Gorgucci, L. Baldini, and A. Tokay, 2014: Evaluation of gamma raindrop size distribution assumption through comparison of rain rates of measured and radar-equivalent gamma DSD. *J. Appl. Meteor. Climatol.*, **53**, 1618–1635, https://doi.org/10.1175/JAMC-D-13-0150.1.

Adler, R. F., and Coauthors, 2003: The Version-2 Global Precipitation Climatology Product (GPCP) monthly precipitation analysis (1979–present). *J. Hydrometeor.*, **4**, 1147–1167, https://doi.org/10.1175/1525-7541(2003)004<1147:TVGPCP>2.0.CO;2.

Albrecht, B., and Coauthors, 2019: Cloud System Evolution in the Trades (CSET): Following the evolution of boundary layer cloud systems with the NSF–NCAR GV. *Bull. Amer. Meteor. Soc.*, **100**, 93–121, https://doi.org/10.1175/BAMS-D-17-0180.1.

Andersson, A., C. Klepp, K. Fennig, S. Bakan, H. Grassl, and J. Schulz, 2011: Evaluation of HOAPS-3 ocean surface freshwater flux components. *J. Appl. Meteor. Climatol.*, **50**, 379–398, https://doi.org/10.1175/2010JAMC2341.1.

Atlas, D., and C. W. Ulbrich, 1974: The physical basis for attenuation–rainfall relationships and the measurement of rainfall parameters by combined attenuation and radar methods. *J. Rech. Atmos.*, **8**, 275–298.

Ayers, G. P., J. M. Cainey, R. W. Gillett, and J. P. Ivey, 1997: Atmospheric sulphur and cloud condensation nuclei in marine air in the Southern Hemisphere. *Philos. Trans. Roy. Soc.*, **B 352**, 203–211, https://doi.org/10.1098/rstb.1997.0015.

Bartholomew, M. J., 2020: Two-dimensional video disdrometer (VDIS) instrument handbook. ARM User Facility Tech. Rep. DOE/SC-ARM-TR-111, 18 pp., https://www.arm.gov/publications/tech_reports/handbooks/vdis_handbook.pdf.

Behrangi, A., and Y. Song, 2020: A new estimate for oceanic precipitation amount and distribution using complementary precipitation observations from space and comparison with GPCP. *Environ. Res. Lett.*, **15**, 124042, https://doi.org/10.1088/1748-9326/abc6d1.

——, and Coauthors, 2016: Status of high-latitude precipitation estimates from observations and reanalyses. *J. Geophys. Res. Atmos.*, **121**, 4468–4486, https://doi.org/10.1002/2015JD024546.

Beusch, L., L. Foresti, M. Gabella, and U. Hamann, 2018: Satellite-based rainfall retrieval: From generalized linear models to artificial neural networks. *Remote Sens.*, **10**, 939, https://doi.org/10.3390/rs10060939.

Bodas-Salcedo, A., and Coauthors, 2014: Origins of the solar radiation biases over the Southern Ocean in CFMIP2 models. *J. Climate*, **27**, 41–56, https://doi.org/10.1175/JCLI-D-13-00169.1.

Bringi, V. N., G.-J. Huang, V. Chandrasekar, and E. Gorgucci, 2002: A methodology for estimating the parameters of a gamma raindrop size distribution model from polarimetric radar data: Application to a squall-line event from the TRMM/Brazil campaign. *J. Atmos. Oceanic Technol.*, **19**, 633–645, https://doi.org/10.1175/1520-0426(2002)019<0633:AMFETP>2.0.CO;2.

——, M. Grecu, A. Protat, M. Thurai, and C. Klepp, 2021: Measurements of rainfall rate, drop size distribution, and variability at middle and higher latitudes: Application to the combined DPR-GMI algorithm. *Remote Sens.*, **13**, 2412, https://doi.org/10.3390/rs13122412.

Bumke, K., G. König-Langlo, J. Kinzel, and M. Schröder, 2016: HOAPS and ERA-Interim precipitation over the sea: Validation against shipboard in situ measurements. *Atmos. Meas. Tech.*, **9**, 2409–2423, https://doi.org/10.5194/amt-9-2409-2016.

Burdanowitz, J., C. Klepp, and S. Bakan, 2016: An automatic precipitation-phase distinction algorithm for optical disdrometer data over the global ocean. *Atmos. Meas. Tech.*, **9**, 1637–1652, https://doi.org/10.5194/amt-9-1637-2016.

——, ——, ——, and S. A. Buehler, 2018: Towards an along-track validation of HOAPS precipitation using OceanRAIN optical disdrometer data over the Atlantic Ocean. *Quart. J. Roy. Meteor. Soc.*, **144**, 235–254, https://doi.org/10.1002/qj.3248.

Chen, H., V. Chandrasekar, H. Tan, and R. Cifelli, 2019: Rainfall estimation from ground radar and TRMM precipitation radar using hybrid deep neural networks. *Geophys. Res. Lett.*, **46**, 10 669–10 678, https://doi.org/10.1029/2019GL084771.

Clough, S. A., and Coauthors, 2005: Atmospheric radiative transfer modeling: A summary of the AER codes. *J. Quant. Spectrosc. Radiat. Transfer*, **91**, 233–244, https://doi.org/10.1016/j.jqsrt.2004.05.058.

Duncan, D. I., C. D. Kummerow, and V. Petkovic, 2018: Towards variational retrieval of warm rain from passive microwave observations. *Atmos. Meas. Tech.*, **11**, 4389–4411, https://doi.org/10.5194/amt-11-4389-2018.

Durden, S. L., Z. S. Haddad, A. Kitiyakara, and F. K. Li, 1998: Effects of nonuniform beam filling on rain retrieval for the TRMM precipitation radar. *J. Atmos. Oceanic Technol.*, **15**, 635–646, https://doi.org/10.1175/1520-0426(1998)015<0635:EONBFO>2.0.CO;2.

Dzambo, A. M., T. L'Ecuyer, O. O. Sy, and S. Tanelli, 2019: The observed structure and precipitation characteristics of southeast Atlantic stratocumulus from airborne radar during ORACLES 2016–17. *J. Appl. Meteor. Climatol.*, **58**, 2197–2215, https://doi.org/10.1175/JAMC-D-19-0032.1.

——, and Coauthors, 2021: Joint cloud water path and rainwater path retrievals from airborne ORACLES observations. *Atmos. Chem. Phys.*, **21**, 5513–5532, https://doi.org/10.5194/acp-21-5513-2021.

Elsaesser, G. S., C. W. O'Dell, M. D. Lebsock, R. Bennartz, T. J. Greenwald, and F. J. Wentz, 2017: The Multisensor Advanced Climatology of Liquid Water Path (MAC-LWP). *J. Climate*, **30**, 10 193–10 210, https://doi.org/10.1175/JCLI-D-16-0902.1.

Giangrande, S. E., D. Wang, M. J. Bartholomew, M. P. Jensen, D. B. Mechem, J. C. Hardin, and R. Wood, 2019: Midlatitude oceanic cloud and precipitation properties as sampled by the ARM Eastern North Atlantic Observatory. *J. Geophys. Res. Atmos.*, **124**, 4741–4760, https://doi.org/10.1029/2018JD029667.

Gras, J. L., 1995: CN, CCN, and particle size in Southern Ocean air at Cape Grim. *Atmos. Res.*, **35**, 233–251, https://doi.org/10.1016/0169-8095(94)00021-5.

Graves, C. E., 1993: A model for the beam-filling effect associated with the microwave retrieval of rain. *J. Atmos. Oceanic Technol.*, **10**, 5–14, https://doi.org/10.1175/1520-0426(1993)010<0005:AMFTBF>2.0.CO;2.

Grecu, M., W. S. Olson, S. J. Munchak, S. Ringerud, L. Liao, Z. Haddad, B. L. Kelley, and S. F. Mclaughlin, 2016: The GPM combined algorithm. *J. Atmos. Oceanic Technol.*, **33**, 2225–2245, https://doi.org/10.1175/JTECH-D-16-0019.1.

Greenwald, T. L., R. Bennartz, M. Lebsock, and J. Teixeira, 2018: An uncertainty data set for passive microwave satellite observations of warm cloud liquid water path. *J. Geophys. Res. Atmos.*, **123**, 3668–3687, https://doi.org/10.1002/2017JD027638.

Grossklaus, M., K. Uhlig, and L. Hasse, 1998: An optical disdrometer for use in high wind speeds. *J. Atmos. Oceanic Technol.*, **15**, 1051–1059, https://doi.org/10.1175/1520-0426(1998)015<1051:AODFUI>2.0.CO;2.

Haynes, J. M., R. T. Marchand, Z. Lou, A. Bodas-Salcedo, and G. L. Stephens, 2007: A multipurpose radar simulation package: QuickBeam. *Bull. Amer. Meteor. Soc.*, **88**, 1723–1728, https://doi.org/10.1175/BAMS-88-11-1723.

——, T. S. L'Ecuyer, G. L. Stephens, S. D. Miller, C. Mitrescu, N. B. Wood, and S. Tanelli, 2009: Rainfall retrieval over the ocean with spaceborne W-band radar. *J. Geophys. Res.*, **114**, D00A22, https://doi.org/10.1029/2008JD009973.

Hilburn, K. A., and F. J. Wentz, 2008: Intercalibrated passive microwave rain products from the Unified Microwave Ocean Retrieval Algorithm (UMORA). *J. Appl. Meteor. Climatol.*, **47**, 778–794, https://doi.org/10.1175/2007JAMC1635.1.

Hou, A. Y., and Coauthors, 2014: The Global Precipitation Measurement mission. *Bull. Amer. Meteor. Soc.*, **95**, 701–722, https://doi.org/10.1175/BAMS-D-13-00164.1.

Humphries, R. S., and Coauthors, 2021: Southern Ocean latitudinal gradients of cloud condensation nuclei. *Atmos. Chem. Phys.*, **21**, 12 757–12 782, https://doi.org/10.5194/acp-21-12757-2021.

Hyder, P., and Coauthors, 2018: Critical Southern Ocean climate model biases traced to atmospheric model cloud errors. *Nat. Commun.*, **9**, 3625, https://doi.org/10.1038/s41467-018-05634-2.

Kay, J. E., C. Wall, V. Yettella, B. Medeiros, C. Hannay, P. Caldwell, and C. Bitz, 2016: Global climate impacts of fixing the Southern Ocean shortwave radiation bias in the Community Earth System Model (CESM). *J. Climate*, **29**, 4617–4636, https://doi.org/10.1175/JCLI-D-15-0358.1.

Kazumori, M., and S. J. English, 2015: Use of the ocean surface wind direction signal in microwave radiance assimilation. *Quart. J. Roy. Meteor. Soc.*, **141**, 1354–1375, https://doi.org/10.1002/qj.2445.

Kidd, C., E. Graham, T. Smyth, and M. Gill, 2021: Assessing the impact of light/shallow precipitation retrievals from satellite-based observations using surface radar and micro rain radar observations. *Remote Sens.*, **13**, 1708, https://doi.org/10.3390/rs13091708.

Klepp, C., 2015: The oceanic shipboard precipitation measurement network for surface validation—OceanRAIN. *Atmos. Res.*, **163**, 74–90, https://doi.org/10.1016/j.atmosres.2014.12.014.

——, K. Bumke, S. Bakan, and P. Bauer, 2010: Ground validation of oceanic snowfall detection in satellite climatologies during LOFZY. *Tellus*, **62A**, 469–480, https://doi.org/10.1111/j.1600-0870.2010.00459.x.

——, and Coauthors, 2018: OceanRAIN, a new in-situ shipboard global ocean surface-reference dataset of all water cycle components. *Sci. Data*, **5**, 180122, https://doi.org/10.1038/sdata.2018.122.

Koistinen, J., and E. Saltikoff, 1998: Experience of customer products of accumulated snow, sleet and rain. *COST 75 Advanced Weather Radar Systems*, European Commission, 397–406, https://op.europa.eu/en/publication-detail/-/publication/404fb559-9d41-4002-a7e0-9a08c81fd264.

Kubar, T. L., D. L. Hartmann, and R. Wood, 2009: Understanding the importance of microphysics and macrophysics for warm rain in marine low clouds. Part I: Satellite observations. *J. Atmos. Sci.*, **66**, 2953–2972, https://doi.org/10.1175/2009JAS3071.1.

Lebsock, M. D., 2018: Level 2C RAIN-PROFILE product process description and interface control document. JPL Tech. Rep. D-20308, 15 pp., https://www.cloudsat.cira.colostate.edu/cloudsat-static/info/dl/2c-rain-profile/2C-RAIN-PROFILE_PDICD.P1_R05.rev0_.pdf.

——, and T. S. L'Ecuyer, 2011: The retrieval of warm rain from *CloudSat. J. Geophys. Res.*, **116**, D20209, https://doi.org/10.1029/2011JD016076.

——, and K. Suzuki, 2016: Uncertainty characteristics of total water path retrievals in shallow cumulus derived from spaceborne radar/radiometer integral constraints. *J. Atmos. Oceanic Technol.*, **33**, 1597–1609, https://doi.org/10.1175/JTECH-D-16-0023.1.

Lee, G. W., and I. Zawadzki, 2005: Variability of drop size distributions: Time-scale dependence of the variability and its effects on rain estimation. *J. Appl. Meteor. Climatol.*, **44**, 241–255, https://doi.org/10.1175/JAM2183.1.

Liao, L., R. Meneghini, and A. Tokay, 2014: Uncertainties of GPM DPR rain estimates caused by DSD parameterizations. *J. Appl. Meteor. Climatol.*, **53**, 2524–2537, https://doi.org/10.1175/JAMC-D-14-0003.1.

——, ——, T. Iguchi, and A. Tokay, 2020: Characteristics of DSD bulk parameters: Implication for radar rain retrieval. *Atmosphere*, **11**, 670, https://doi.org/10.3390/atmos11060670.

Mace, G. G., S. Avey, S. Cooper, M. Lebsock, S. Tanelli, and G. Dobrowalski, 2016: Retrieving co-occurring cloud and precipitation properties of warm marine boundary layer clouds with A-Train data. *J. Geophys. Res. Atmos.*, **121**, 4008–4033, https://doi.org/10.1002/2015JD023681.

Marshall, J., and W. M. Palmer, 1948: The distribution of raindrops with size. *J. Meteor.*, **5**, 165–166, https://doi.org/10.1175/1520-0469(1948)005<0165:TDORWS>2.0.CO;2.

McFarquhar, G. M., and Coauthors, 2021: Observations of clouds, aerosols, precipitation, and surface radiation over the Southern Ocean: An overview of CAPRICORN, MARCUS, MICRE, and SOCRATES. *Bull. Amer. Meteor. Soc.*, **102**, E894–E928, https://doi.org/10.1175/BAMS-D-20-0132.1.

Mie, G., 1908: Beiträge zur Optik trüber Medien, speziell kolloidaler Metallösungen. *Ann. Phys.*, **330**, 377–445, https://doi.org/10.1002/andp.19083300302.

Miller, D. J., Z. Zhang, A. S. Ackerman, S. Platnick, and B. A. Baum, 2016: The impact of cloud vertical profile on liquid water path retrieval based on the bispectral method: A theoretical study based on large-eddy simulations of shallow marine boundary layer clouds. *J. Geophys. Res. Atmos.*, **121**, 4122–4141, https://doi.org/10.1002/2015JD024322.

Minzner, R. A., 1977: The 1976 Standard Atmosphere and its relationship to earlier standards. *Rev. Geophys.*, **15**, 375–384, https://doi.org/10.1029/RG015i003p00375.

Mülmenstädt, J., O. Sourdeval, J. Delanoë, and J. Quaas, 2015: Frequency of occurrence of rain from liquid-, mixed-, and ice-phase clouds derived from A-Train satellite retrievals. *Geophys. Res. Lett.*, **42**, 6502–6509, https://doi.org/10.1002/2015GL064604.

——, and Coauthors, 2021: An underestimated negative cloud feedback from cloud lifetime changes. *Nat. Climate Change*, **11**, 508–513, https://doi.org/10.1038/s41558-021-01038-1.

National Academies of Science, Engineering, and Medicine, 2018: *Thriving on Our Changing Planet: A Decadal Strategy for Earth Observation from Space.* National Academies Press, 716 pp., https://doi.org/10.17226/24938.

Nelson, E. S., and T. S. L'Ecuyer, 2018: Global character of latent heat release in oceanic warm rain systems. *J. Geophys. Res. Atmos.*, **123**, 4797–4817, https://doi.org/10.1002/2017JD027844.

Nuijens, L., K. Emanuel, H. Masunaga, and T. L'Ecuyer, 2017: Implications of warm rain in shallow cumulus and congestus clouds for large-scale circulations. *Surv. Geophys.*, **38**, 1257–1282, https://doi.org/10.1007/s10712-017-9429-z.

Posselt, D. J., J. Kessler, and G. G. Mace, 2017: Bayesian retrievals of vertically resolved cloud particle size distribution properties. *J. Appl. Meteor. Climatol.*, **56**, 745–765, https://doi.org/10.1175/JAMC-D-16-0276.1.

Protat, A., C. Klepp, V. Louf, W. A. Petersen, S. P. Alexander, A. Barros, J. Leinonen, and G. G. Mace, 2019a: The latitudinal variability of oceanic rainfall properties and its implication for satellite retrievals: 1. Drop size distribution properties. *J. Geophys. Res. Atmos.*, **124**, 13 291–13 311, https://doi.org/10.1029/2019JD031010.

——, ——, ——, ——, ——, ——, ——, and ——, 2019b: The latitudinal variability of oceanic rainfall properties and its implication for satellite retrievals: 2. The relationships between radar observables and drop size distribution parameters. *J. Geophys. Res. Atmos.*, **124**, 13 312–13 324, https://doi.org/10.1029/2019JD031011.

Redemann, J., and Coauthors, 2021: An overview of the ORACLES (ObseRvations of Aerosols above CLouds and their intEractionS) project: Aerosol–cloud–radiation interactions in the southeast Atlantic basin. *Atmos. Chem. Phys.*, **21**, 1507–1563, https://doi.org/10.5194/acp-21-1507-2021.

Rodgers, C. D., 2000: *Inverse Methods for Atmospheric Sounding: Theory and Practice.* World Science, 240 pp.

Sarkar, M., P. Zuidema, B. Albrecht, V. Ghate, J. Jensen, J. Mohrmann, and R. Wood, 2020: Observations pertaining to precipitation within the northeast Pacific stratocumulus-to-cumulus transition. *Mon. Wea. Rev.*, **148**, 1251–1273, https://doi.org/10.1175/MWR-D-19-0235.1.

——, ——, and V. Ghate, 2021: Clarifying remotely retrieved precipitation of shallow marine clouds from the NSF/NCAR Gulfstream V. *J. Atmos. Oceanic Technol.*, **38**, 1657–1670, https://doi.org/10.1175/JTECH-D-20-0166.1.

Schulte, R. M., and C. D. Kummerow, 2019: An optimal estimation retrieval algorithm for microwave humidity sounding channels with minimal scan position bias. *J. Atmos. Oceanic Technol.*, **36**, 409–425, https://doi.org/10.1175/JTECH-D-18-0133.1.

——, ——, W. Berg, S. C. Reising, S. T. Brown, T. C. Gaier, B. H. Lim, and S. Padmanabhan, 2020: An passive microwave retrieval algorithm with minimal view-angle bias: Application to the TEMPEST-D CubeSat Mission. *J. Atmos. Oceanic Technol.*, **37**, 197–210, https://doi.org/10.1175/JTECH-D-19-0163.1.

Seto, S., and T. Iguchi, 2015: Intercomparison of attenuation correction methods for the GPM dual-frequency precipitation radar. *J. Atmos. Oceanic Technol.*, **32**, 915–926, https://doi.org/10.1175/JTECH-D-14-00065.1.

——, ——, R. Meneghini, J. Awaka, T. Kubota, T. Masaki, and N. Takahashi, 2021: The precipitation rate retrieval algorithms for the GPM Dual-frequency Precipitation Radar. *J. Meteor. Soc. Japan*, **99**, 205–237, https://doi.org/10.2151/jmsj.2021-011.

Sinclair, K., B. van Diedenhoven, B. Cairns, M. Alexandrov, A. M. Dzambo, and T. L'Ecuyer, 2021: Inference of precipitation in warm stratiform clouds using remotely sensed observations of cloud top droplet size distribution. *Geophys. Res. Lett.*, **48**, e2021GL092547, https://doi.org/10.1029/2021GL092547.

Stephens, G. L., and C. D. Kummerow, 2007: The remote sensing of clouds and precipitation from space: A review. *J. Atmos. Sci.*, **64**, 3742–3765, https://doi.org/10.1175/2006JAS2375.1.

——, and Coauthors, 2002: The *CloudSat* mission and the A-Train. *Bull. Amer. Meteor. Soc.*, **83**, 1771–1790, https://doi.org/10.1175/BAMS-83-12-1771.

——, and Coauthors, 2012: An update on Earth's energy balance in light of the latest global observations. *Nat. Geosci.*, **5**, 691–696, https://doi.org/10.1038/ngeo1580.

Stubenrauch, C. J., and Coauthors, 2013: Assessment of global cloud datasets from satellites: Project and database initiated by the GEWEX radiation panel. *Bull. Amer. Meteor. Soc.*, **94**, 1031–1049, https://doi.org/10.1175/BAMS-D-12-00117.1.

Tanelli, S., S. Durden, E. Im, K. Pak, D. G. Reinke, P. Partain, and J. M. Haynes, 2008: *CloudSat*'s cloud profiling radar after two years in orbit: Performance, calibration, and processing. *IEEE Trans. Geosci. Remote Sens.*, **46**, 3560–3573, https://doi.org/10.1109/TGRS.2008.2002030.

Tang, G., D. Long, A. Behrangi, C. Wang, and Y. Hong, 2018: Exploring deep neural networks to retrieve rain and snow in high latitudes using multisensory and reanalysis data. *Water Resour. Res.*, **54**, 8253–8278, https://doi.org/10.1029/2018WR023830.

Testud, J., S. Oury, R. A. Black, P. Amayenc, and X. Dou, 2001: The concept of "normalized" distribution to describe raindrop spectra: A tool for cloud physics and cloud remote sensing. *J. Appl. Meteor. Climatol.*, **40**, 1118–1140, https://doi.org/10.1175/1520-0450(2001)040<1118:TCONDT>2.0.CO;2.

Thurai, M., and V. N. Bringi, 2018: Application of the generalized gamma model to represent the full rain drop size distribution spectra. *J. Appl. Meteor. Climatol.*, **57**, 1197–1210, https://doi.org/10.1175/jamc-d-17-0235.1.

Tokay, A., and P. G. Bashor, 2010: An experimental study of small-scale variability of raindrop size distribution. *J. Appl. Meteor. Climatol.*, **49**, 2348–2365, https://doi.org/10.1175/2010JAMC2269.1.

Trenberth, K. E., and J. T. Fasullo, 2010: Simulation of present-day and twenty-first-century energy budgets of the Southern Oceans. *J. Climate*, **23**, 440–454, https://doi.org/10.1175/2009JCLI3152.1.

van de Beek, C. Z., H. Leijnse, P. Hazenberg, and R. Uijlenjoet, 2016: Close-range radar rainfall estimation and error analysis. *Atmos. Meas. Tech.*, **9**, 3837–3850, https://doi.org/10.5194/amt-9-3837-2016.

Witte, M. K., T. Yuan, P. Y. Chuang, S. Platnick, K. G. Meyer, G. Wind, and H. H. Jonsson, 2018: MODIS retrievals of cloud effective radius in marine stratocumulus exhibit no significant bias. *Geophys. Res. Lett.*, **45**, 10656–10664, https://doi.org/10.1029/2018GL079325.

Wood, R., 2005: Drizzle in stratiform boundary layer clouds. Part II: Microphysical aspects. *J. Atmos. Sci.*, **62**, 3034–3050, https://doi.org/10.1175/JAS3530.1.

Xu, Z., G. G. Mace, and D. J. Posselt, 2019: A method for assessing relative skill in retrieving cloud and precipitation properties in next-generation cloud radar and radiometer orbiting observatories. *J. Atmos. Oceanic Technol.*, **36**, 2283–2306, https://doi.org/10.1175/JTECH-D-18-0204.1.

Yang, F., E. P. Luke, P. Kollias, A. B. Kostinski, and A. M. Vogelmann, 2018: Scaling of drizzle virga depth with cloud thickness for marine stratocumulus clouds. *Geophys. Res. Lett.*, **45**, 3746–3753, https://doi.org/10.1029/2018GL077145.

Zelinka, M. D., T. A. Myers, D. T. McCoy, S. Po-Chedley, P. M. Caldwell, P. Ceppi, S. A. Klein, and K. E. Taylor, 2020: Causes of higher climate sensitivity in CMIP6 models. *Geophys. Res. Lett.*, **47**, e2019GL085782, https://doi.org/10.1029/2019GL085782.

Zhang, L., D. Lu, S. Duan, and J. Liu, 2004: Small-scale rain nonuniformity and its effect on evaluation of nonuniform beam-filling error for spaceborne radar rain measurement. *J. Atmos. Oceanic Technol.*, **21**, 1190–1197, https://doi.org/10.1175/1520-0426(2004)021<1190:SRNAIE>2.0.CO;2.